Development of a Dual-Joint Harmonic Drive Actuator Robotic Arms System for Compliant Motion Control

Wen-Hao Chen, Yu-Han Tsai, and Chun-Yeon Lin, *Member, RST*

***Abstract*—This paper presents the development of a dual-joint robotic arm with harmonic drive actuators (HDA) for compliant motion control and accurate torque estimation. A flexible joint model is proposed to estimate the dynamic motion of the robotic arm. Torque and displacement (T-D) sensors are developed and placed at the joints of the harmonic drive to estimate the torque value by reading the output angle of the load side, accounting for kinematic torsion compensation. Impedance and admittance control strategies are investigated through simulations to enhance safety during human-robot interaction, and the effects of various parameters on the system are investigated through simulations. The prototype of a robotic arm has been developed. The robotic arm is given specific working paths to simulate working scenarios in both simulations and experiments. External disturbances are applied to observe the two controllers' compliance and position-tracking capabilities.**

***Index Terms*—Harmonic drive, compliant motion control, human-robot interaction**

I. INTRODUCTION

Harmonic drive actuators (HDA) employ a unique speed reduction mechanism comprising circular and flex splines. The wave generator actively induces deformation in the flex spline, which in turn engages and drives the rotation of the circular spline. The HDA, featured by its high precision, zero backlashes, and compact design, is widely used in robotics arms [1]. Since robotic arms are increasingly widely used in the working space with humans, the safety of human-robot interaction rises. Several techniques have been developed to address this difficulty. Torque estimation is crucial in this situation. A method with an optical torque sensor is developed, enabling torque measurement in each joint [2]. In addition, another strategy exploiting torque estimation can detect collisions to enhance the safety of human-robot interaction [3]. Compliance control is an approach that makes the system react to external disturbances from the environment [4] instead of the given positions. Several strategies are applied to achieve compliance control, including neuron networks [5], stability-based [6], and model-dynamic-based approaches [7]. Related applications involve human-robot cooperation for lower limb exoskeletons assisting human walking [8]−[11]. Huang et al. proposed a position-based compliance control model for collaborative robots to correct the disturbance from external forces [12]. A variable control framework based on virtual fixtures is proposed to assist humans in heavy duties [13]. Gongming et al. have developed a method based on compliance control to capture targets with a multi-arm free-flying space robot [14].

A comprehensive dynamic model is necessary to precisely estimate the torque and control HDA. Initially, Masoumi et al. proposed a preliminary HDA dynamic model that does not consider the soft effects of the HDA, which causes a lower estimated value of transmitted torque than the actual value. Subsequently, several scholars have considered the effects of flexibility, friction, and hysteresis and formulated appropriate mathematical models [15] − [18]. In addition, a more sophisticated model concerns torsion-torque and nonlinear friction [19]. This research applied dynamic models in [20], [21] to estimate the energy consumption by the hysteresis effect from the wave generator and the flex spline. The error caused by the hysteresis effect that a disturbance observer can compensate for was discussed in [22]. Moreover, the Kalman filter can be incorporated to reduce measuring noise [23].

Torque meters are commonly used to measure the torque generated by loads. However, this approach costs more and requires more complicated robotic arms design. Several estimation methods using strain gauges and encoders are proposed as improved alternatives. These methods apply the observation of the deformation from the flex splines. Another method uses encoders to measure the torsional angles and then estimates torque by a simplified linear model [24]. A comparison study of strain gauge and encoder-based methods has been conducted [25]. Estimation methods based on strain gauges can be more robust under non-axial disturbance and vibration. Nonetheless, analog to digital conversion is prone to influence strain gauge sensors. Encoder-based methods only need to consider the sampling rate of the encoders.

Several disturbances must be considered to obtain a precise torque estimation model. One is the additional torque by the weight of the end-effectors. This disturbance can be reduced by adding bearings. Another disturbance is caused by the vibration, which originates from the sinusoidal effects of the flex spline during rotation [26]. The Kalman filter filters out the redundant torque ripples [27]. Another modified strain gauge configuration built in the Wheatstone bridge is proposed to minimize the oscillations [28]. The admittance and impedance control are the common methods for the human-robot interaction. Yamada et al. compared these two methods by controlling a multi-finger-arm robot [29].

Dual-joint robots, which have two rotary joints in each of their arms, offer unique advantages that enhance their versatility, dexterity, and flexibility in various applications.

This work was supported by Higher Education Sprout Project, Taiwan, under Grant NTU-CC-107L891001 and NTU-CC-108L891001. (Corresponding author: Chun-Yeon Lin.)

Yu-Han Tsai and Chun-Yeon Lin are with the Department of Mechanical Engineering, National Taiwan University, Taipei 10617, Taiwan. (e-mail: d12522006@ntu.edu.tw; chunyeonlin@ntu.edu.tw)

Wen-Hao Chen was with the Department of Mechanical Engineering, National Taiwan University, Taipei 10617, Taiwan. He is now with Taiwan Semiconductor Manufacturing Company. (e-mail: bensonok456@gmail.com)

Manuscript received 15 October 2024; revised 21 December 2024; accepted 14 January 2025; Date of publication 21 January 2025.

This paper proposes a development process for developing a dual-joint harmonic drive actuator robotic arms system and implementing compliant control to slow down obstacle collisions. The optical encoder measures the angular displacement to estimate the torque.

The remainder of this paper provides the following:

- The dynamic model that describes the dual-joint HDA is presented. A sensor-less torque estimation method used in compliance control is developed and validated by the torque sensor. Two compliance control methods are discussed and implemented on the HDA robotic system.
- Numerical simulation of the dynamic model, torque estimation method, and compliance control methods are conducted. A self-designed dual-joint robotic arm based on the HDA is utilized to validate the proposed methods experimentally.

II. A DUAL-JOINT HARMONIC DRIVE ACTUATOR SYSTEM DESIGN

Fig. 1 illustrates the proposed design of a dual-joint robotic arm design with a HDA. DC motors drive the robotic arm. A side view of the designed system is shown in Fig. 1(a). The rotary encoder is located at the joint of the robotic arms to measure the torsion displacement. A torque sensor is installed at the end-effector to derive the applied torque on the input handle. The measurement from the torque sensor is used to validate the torque estimation method. Fig. 1(b) shows the system modules to realize compliance control and validate the feasibility of the proposed dynamic model and torque estimation method.

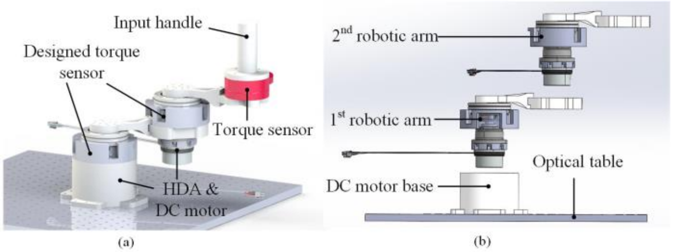

Fig. 1. A dual-joint system configuration. (a) Illustration of the location of the sensors (b) System modules.

A. HDA system dynamic model & torque estimation

Fig. 2 illustrates the HDA model, composed of a wave generator, flex spline, and circular spline. The relationship of the angular displacement of wave generator θ_w, flex spline θ_f, and circular spline θ_{cs} is described by

$$\theta_w = (N+1)\theta_{cs} - N\theta_f \tag{1}$$

,where N is the reduction ratio between the wave generator and flex spline.

Since the circular spline is fixed on the base, θ_{cs} is zero. The relationship between wave generator torque τ_w and flex spline torque τ_f is:

$$\tau_w = -\frac{1}{N}\tau_f \,. \tag{2}$$

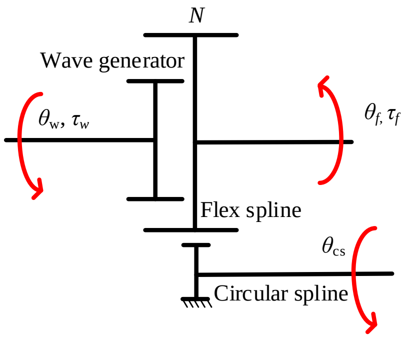

Fig. 2. Illustration of the ideal HDA model mechanism.

Due to the flexibility of the wave generator and the flex spline, the input and output angles in each component are inconsistent. A more sophisticated model incorporating elastic coefficients K_w and K_f is introduced, as depicted in Fig. 3(a). The model also considers the friction and hysteresis effects between the wave generator and the flex spline to reflect real-world conditions accurately.

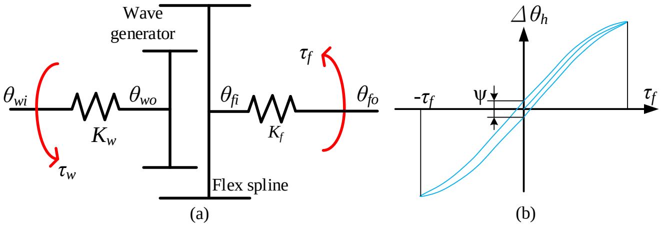

Fig. 3. HDA dynamic model involving soft effect. (a) HDA mechanism. (b) Hysteresis effect.

$$K_\ell = \frac{d\tau_\ell}{d\Delta\theta_\ell} \tag{3}$$

The definition of the elastic coefficients of K_w and K_f are shown in (3), where $\ell \in w, f$. Ψ is the hysteresis loss as shown in Fig. 3(b). The hysteresis effect results in a variable elastic coefficient K_w, which can be modeled as an exponential function. The elastic coefficient K_w is defined as (4); K_{w0} is the initial elastic coefficient when the applied torque is zero; θ_{wi} and θ_{wo} are the input and output angular displacements of the wave generator

$$K_w = K_{w0} e^{-c_w|\tau_w|} \tag{4}$$

$$\Delta\theta_w = \int \frac{d\tau_w}{K_w}, \text{ where } \Delta\theta_w = \theta_{wi} - \theta_{wo} \,. \tag{5}$$

Using (3), $\Delta\theta_w$ is written into the integral form, represented as (5). By substituting (3) into (4), $\Delta\theta_w$ is obtained b

$$\Delta\theta_w = \frac{\mathrm{sign}(\tau_w)}{c_w K_{w0}}\left(1 - e^{-c_w|\tau_w|}\right). \tag{6}$$

The friction between the flex spline and the wave generator causes the hysteresis effect, as shown in Fig. 3(b). $\Delta\theta_h$ represents the total deformation of the HDA used to model the hysteresis effect, which is given by (7). The hysteresis effect allows the torque generated by the flex spline τ_f estimated by

$$\Delta\theta_h = \Delta\theta_f - \Delta\theta_w / N \,; \tag{7}$$

$$\tau_f = d_1 \Delta\theta_h + d_3 \Delta\theta_h^{\,3} \,, \tag{8}$$

where d_1 and d_3 are constants to be determined.

The relationship of $\Delta\theta_h$ and $\Delta\theta_f$ is shown in (7). Since the derivative of $\Delta\theta_h$ is the same as $\Delta\theta_f$. K_f is derived by differentiating (8) with $\Delta\theta_f$, which is shown as follows:

$$K_f = \frac{d\tau_f}{d\theta_f} = K_{f0}\left[1+\left(c_f\theta_f\right)^2\right], \tag{9}$$

where c_f and K_{f0} denote the constant to be determined.

Using (4) and (9), $\Delta\theta_f$ is derived by (10). $\Delta\theta_h$ is derived in (11) by substituting (7) and (10) into (3)

$$\Delta\theta_f = \frac{\arctan(c_f\tau_f)}{c_f K_{f0}}, \text{ where } \Delta\theta_f = \theta_{fi} - \theta_{fo}; \tag{10}$$

$$\Delta\theta_h = \frac{\arctan(c_f\tau_f)}{c_f K_{f0}} - \frac{\operatorname{sign}(\tau_w)}{c_w N K_{w0}}\left(1 - e^{-c_w|\tau_w|}\right) \tag{11}$$

where the constants of c_f, c_w, K_{f0}, K_{w0} are provided by the HDA manufacturer.

Conventional methods integrate torque sensors within the wave generator and the flex spline, increasing the system's cost and complexity. This proposed method eliminates the need for additional torque sensors. The torsional angles ($\Delta\theta_h$, θ_{wo}, θ_{fi}) within the HDA system are not directly measured. The known angular displacements (θ_{wi}, θ_{fo}) are used to overcome this difficulty. The total torsional angle $\Delta\theta$ of the HDA is obtained, which is shown as follows:

$$\Delta\theta = \theta_{fo} + \frac{\theta_{wi}}{N}; \tag{12}$$

where θ_{fo} is equal to the output angle from the motor, measured from the motor's encoder; θ_{wi} is obtained from the optical encoder from the end-effector. While the motor is rotating, a periodical angular displacement fluctuation occurs [30]. The phenomenon originates from the tolerance of the motor assembly. To accurately determine the pure movement of the HDA represented as kinematic torsion, a fifth-order polynomial of the end-effector's angular displacement is used to model the actual angular displacement by filtering out other torsion variation, as shown as follows:

$$\Delta\theta_t = \sum_{k=0}^{5} a_k\theta^k \tag{13}$$

where coefficients of the polynomial a_k are derived by fitting the experimental data from the torsional angle of the end-effector.

The HDA deformation $\Delta\theta_h$ is derived by subtracting kinematic torsion $\Delta\theta_t$ from the total torsional angle $\Delta\theta$

$$\Delta\theta_h = \Delta\theta - \Delta\theta_t. \tag{14}$$

With (14), (7) is rewritten as:

$$\Delta\theta_{fk} = \Delta\theta_k - \Delta\theta_{tk} + \frac{\Delta\theta_{wk}}{N}. \tag{15}$$

Then substituting (15) into (10), the estimated torque of the flex spline is obtained

$$\tau_f = \frac{\tan\left[\left(\Delta\theta_k - \Delta\theta_{tk} + \frac{\Delta\theta_{wk}}{N}\right)c_f K_{f0}\right]}{c_f}. \tag{16}$$

In (16), the torsional angle of the wave generator ($\Delta\theta_w$) is known. (6) provides the relationship between τ_w and $\Delta\theta_w$ to determine $\Delta\theta_w$. The function for calculating τ_w is given by

$$\tau_w = \begin{cases} \tau_m - \tau_{fs}, & \tau_m > \tau_{fs} \\ \tau_m + \tau_{fs}, & \tau_m < \tau_{fs} \\ \tau_f / N, & \tau_m = \tau_{fs} \end{cases}. \tag{17}$$

As illustrated in Fig. 3(a), the wave generator connects to both the step motor and the flex spline. When the motor drives the wave generator, τ_w depends on the motor torque τ_m, which can be obtained from reading the values of the motor chip and the torque caused by friction τ_{fs}, which opposes the motor torque. If the motor torque is balanced, namely τ_m equals to τ_{fs}. the flex spline drives τ_w.

B. *Model of the HDA Robotic Arm*

Fig. 4 illustrates the developed model, which includes the DC motors and HDA. The robotic arm consists of two parts: the first is driven by a DC motor, and the second arm serves as an end-effector. J_m and J_a represent the inertia of the motor and arm, respectively. k denotes the k^{th} robotic arm. The torques provided by the DC motor and flex spline are given by

$$\tau_{mk} = J_m\ddot{\theta}_{wok} + r_m\dot{\theta}_{wok} + \tau_{wk} - \tau_{fsk}; \tag{18}$$

$$\tau_{fk} = K_f(\theta_{fok} + \frac{\theta_{wok}}{N}) \tag{19}$$

where $\theta_{wok} = \theta_{mk} + \Delta\theta_{wk}$.

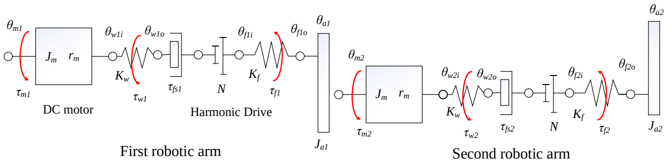

Fig. 4. Dynamic model of the dual-joint HDA arms.

C. *Inverse kinematic of the HDA system*

The proposed HDA robotic arm consists of two segments, which can be modeled as the RR robot depicted in Fig. 5. The motion trajectory of the dual-joint robotic arm is parallel to the ground, and gravitational effects are not considered. The robotic arm attempts to perform compliance control when an external force is applied at point p.

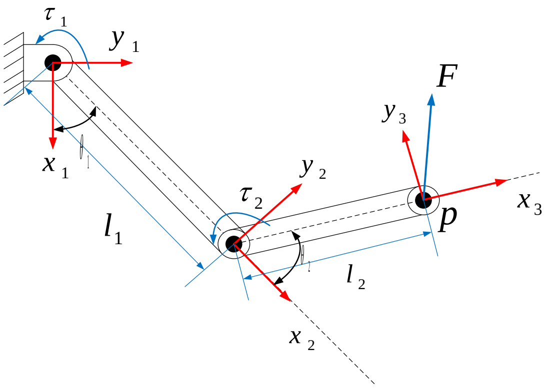

Fig. 5. Dual-joint robotic arm diagram.

The theory of compliance control is established in a Cartesian coordinate system. f_x, f_y represent the external force measured at the end effector in x, y directions; τ_1, τ_2 are the estimated torque at the first and second joints derived in the torque estimation method. The estimated torque from the flex spline calculates the force applied by the external source:

$$\begin{bmatrix} f_x \\ f_y \end{bmatrix} = \begin{bmatrix} l_2 \sin\theta_2 & l_2 + l_1 \cos\theta_2 \\ 0 & l_2 \end{bmatrix}^{-1} \begin{bmatrix} \tau_1 \\ \tau_2 \end{bmatrix}. \tag{20}$$

The inverse kinematic is achieved with the aid of equation (20). The angles between each arm θ_1, θ_2 are given as

$$\theta_1 = \arctan\left(\frac{f_y}{f_x}\right) - \operatorname{arcos}\left(\frac{f_x^{\,2} + f_y^{\,2} + l_1^{\,2} - l_2^{\,2}}{2l_1\sqrt{f_x^{\,2} + f_y^{\,2}}}\right) \tag{21a}$$

$$\theta_2 = \operatorname{arcos}\left(\frac{f_x^{\,2} + f_y^{\,2} - l_1^{\,2} - l_2^{\,2}}{2l_1 l_2}\right). \tag{21b}$$

D. Compliance control of the HDA system

The compliance control methods can be divided into two categories: impedance control and admittance control. The entire HDA robotic arm system is modeled as a mechanical impedance system involving variables such as mass (M), damping (B), and spring constant (K). When an external force is applied, the actual displacement of the robotic arm does not align with the expected trajectory. This discrepancy is equivalent to changes in the system's M, B, and K values. The differential equations modeling is described by

$$\mathbf{F_e} = M\ddot{\mathbf{x}}_\mathbf{e} + B\dot{\mathbf{x}}_\mathbf{e} + K\mathbf{x}_\mathbf{e}\text{, where } \mathbf{x}_\mathbf{e} = [x_d - x, y_d - y]^{\mathrm{T}}; \tag{22}$$

$$\boldsymbol{\tau}_e = M\ddot{\boldsymbol{\theta}}_\mathbf{e} + B\dot{\boldsymbol{\theta}}_\mathbf{e} + K\boldsymbol{\theta}_\mathbf{e}. \tag{23}$$

(x_d, y_d) and (x, y) denote the desired trajectory input and actual position; $\mathbf{F_e}$, $\mathbf{x_e}$ represent the errors in the desired force and position, respectively. τ_e, θ_e denote the torque and position errors in rotational coordinates. The end effector receives the external force in the proposed HDA system. The system dynamic model is simplified to a one-degree-of-freedom system. The equation of motion at the point p is denoted as follows:

$$m\ddot{\mathbf{x}} = \mathbf{F} + \mathbf{F_e} \tag{24}$$

where $\mathbf{F}$ is the force input from the impedance compliance control, and $\mathbf{F_e}$ is the external force; m is the mass of the end effector. Using (22) and (24), the input force for the impedance compliance control is derived as

$$\mathbf{F} = \left(\frac{m}{M} - 1\right)\mathbf{F}_e + m\ddot{\mathbf{x}}_\mathbf{d} - \frac{m}{M}(B\dot{\mathbf{x}}_\mathbf{e} + K\mathbf{x}_\mathbf{e}) \tag{25}$$

where $\mathbf{x_d}$ is the desired position.

Similar to the impedance compliance control method, the admittance compliance control method handles the difference between the expected and actual position. The transfer function of the admittance compliance control method is defined as follows:

$$\mathbf{x_e}(s) = \frac{1}{Ms^2 + Bs + K}\mathbf{F_e}(s). \tag{26}$$

E. Dual-joint HDA system design

Fig. 6 illustrates the dual-joint HDA system composed of a DC motor, HDA, sensor mechanism, bearing, and arm connected to the flange shaft. The flange shaft rotates the arm while the flex spline rotates. The components are made by 3D printing except for the sensor mechanisms, which require high precision. The selection of bearings is based on the load conditions to which they are subjected. Because bearings must withstand axial and radial forces, common ball bearings cannot be used. Instead, designs capable of handling composite loads, such as cross-roller bearings, are required. After considering the load conditions and bearing life calculations, the THK RU66UUCC0 modular bearing is chosen.

Fig. 7(a) illustrates the experimental setup of the angular displacement and torque sensor in the torque estimation experiment. The flange shaft is employed to output the twist angle of the flexible spline, which is connected to an optical disc. Angular displacement information is obtained through an optical encoder reading head. Fig. 6(c) illustrates the force sensor module mounted on the end joint during the dual-joint compliance control experiment. The force applied to the handle can be obtained via the six-axis force and torque sensor and compared with the torque estimation results. Fig. 7(a) shows the side view of the dual-joint HDA, featuring components such as the optical table motor mounting bracket, bearing, arm, and handle, all manufactured using 3D printing. Fig. 7(b) provides an internal view of the angular displacement and torque sensor, where the optical disc and optical encoder are fixed within a specific distance for accurate measurement. The components are fabricated from metal to ensure precision.

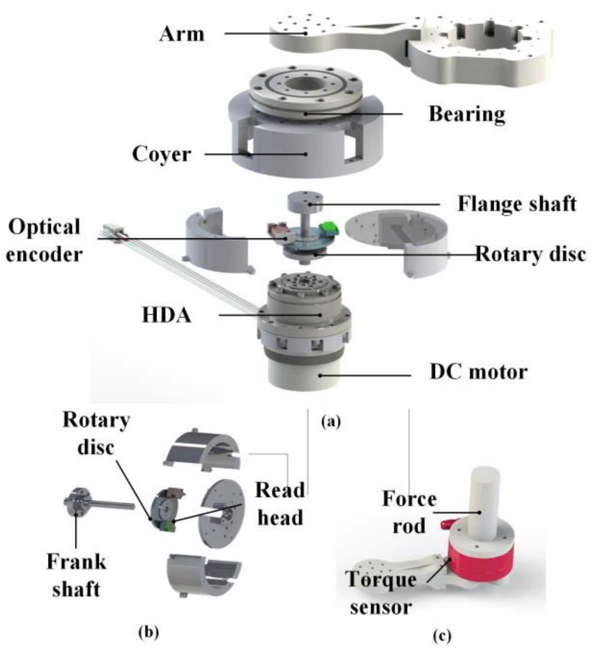

Fig. 6. Schematics of the dual-joint HDA system. (a) Explosive figure of HDA arm. (b) Exploded view of the displacement and torque sensors. (c) Torque sensor module.

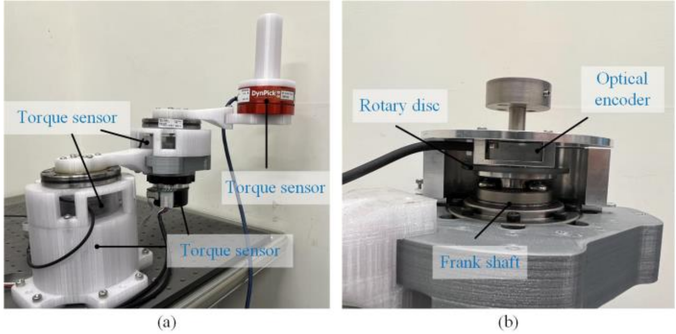

Fig. 7. The setup diagram of the dual-joint HDA robotic arm. (a) Robotic arm. (b) The internal structure of the angular displacement and torque sensor.

III. NUMERICAL VALIDATION OF THE DUAL-JOINT HDA SYSTEM

The dual-joint HDA system can be validated with numerical simulations with three focuses: The calculation of model parameters, numerical validation of torque estimation, and compliance control.

A. Model Parameter Calculation

Parameters of the HDA are determined to establish a correct model. Fig. 8 illustrates the behavior of the stiffness of the HDA. The HDA's modeling parameter refers to the manufacturers' technological report [31]. The elastic coefficient K is divided into three regions to simulate the hysteresis effect. Fig. 8 determines the coefficients c_f and K_{f0} for numerical validation.

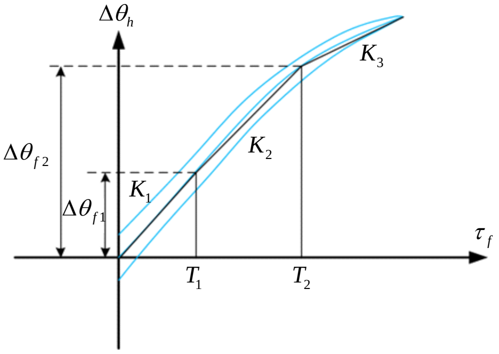

Fig. 8. Stiffness curve of the HAD.

The value of elastic coefficient K depends on the applied torque intervals, marking as $\tau_{f1}\in[0, T_1]$, $\tau_{f2}\in[T_1, T_2]$, and $\tau_{f3}\in[T_2, \infty]$ as shown in Fig. 8. The elastic coefficient K can be obtained by the (27), which derived by substituting τ_{f1} and τ_{f2} into (9)

$$K_n = K_{f0}\left[1+\left(c_f\Delta\theta_{fn}\right)^2\right], \text{ where } n = 1, 2, \text{and } 3\,. \qquad (27)$$

(28) reveals the solved c_f is determined through the solution of (27):

$$c_f = \sqrt{\frac{K_1 - K_2}{K_{fo}(\Delta\theta_{f2}{}^2 - \Delta\theta_{f1}{}^2)}} \qquad (28a)$$

With (9), at the starting point, where τ_f is zero and τ_w is the stiction torque ignoring the hysteresis effect term, K_{w0} is determined as follows:

$$K_{w0} = \frac{2\tau_{fs}}{N\psi}\,. \qquad (29)$$

$\Delta\theta_w$ is derived by (5), which is expressed as follows:

$$\Delta\theta_w = \frac{1}{c_w N K_{w0}}\,. \qquad (30)$$

Therefore, the coefficient c_w is determined as

$$c_w = \frac{2}{\psi N K_{w0}}\,. \qquad (31)$$

B. Numerical Validation of Torque Estimation

The parameter of the model is listed in Table I. The sinusoidal and step input responses of the DC motor are compared.

TABLE I
PARAMETERS OF THE VALIDATION MODEL

J_m (kgm^2)	1.21×10^{-4}	τ_{fs} (Nm)	0.037
J_w (kgm^2)	0.079×10^{-4}	N	100
J_a (kgm^2)	0.876	c_w (1/Nm)	27.027
K_{wo}(Nm/rad)	2.5517	K_f (Nm/rad)	10000
K_{fo} (Nm/rad)	9743.94	c_f (1/Nm)	0.0831
l_a (m)	0.15		

Fig. 9 demonstrates the results of the numerical validation by providing step and sinusoidal inputs to the motors. Peak currents of 2A are applied to the DC motors. The sinusoidal input has a frequency of 1 rad/sec. The torque estimation values are compared with the measurements. The results indicate that the output torque from the first arm is twice as large as the second arm, as the second arm is part of the load for the first arm.

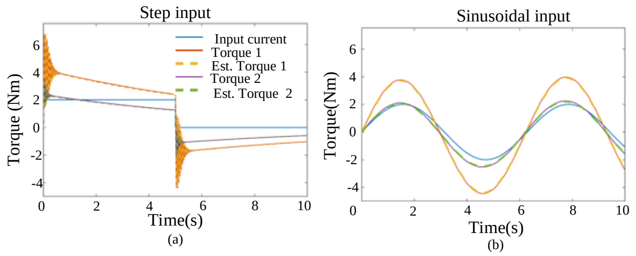

Fig. 9. Numerical validation results for the dual-joint HDA robotic arm. (a) Step input. (b) Sinusoidal input.

C. Numerical Validation of Compliance Control

The parametric effects of applying impedance and admittance compliance control are numerically investigated. Fig. 10 shows the flowchart to evaluate the compliance control methods.

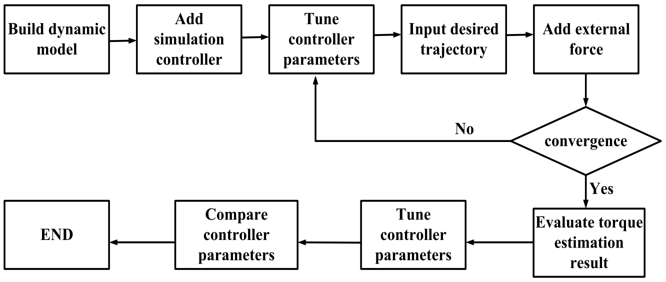

Fig. 10. Illustration of the numerical validation process

The performance of two compliance control methods is compared under identical conditions. The robotic arm executes to follow a circular trajectory with a radius of 5 cm. External forces are applied along the X coordinate from the third to the fourth second and the Y coordinate from the sixth to seventh second.

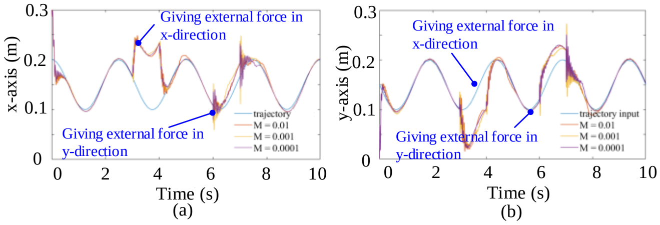

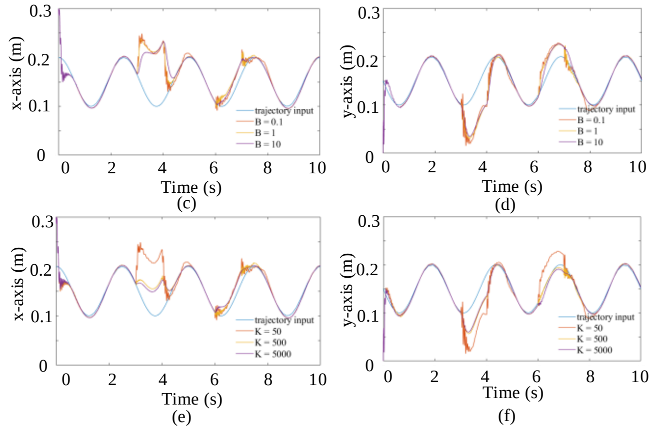

Fig. 11. Responses of the admittance compliance control of adjusting *M*, *B*, *K* parameters. (a)-(b) Adjusting values of *M*. (c)-(d) Adjusting value of *B*. (e)-(f) adjusting value of *K*.

Fig. 11(a)-(f) shows how the parameters (*M*, *B*, and *K*) influence the system response. Fig. 11 (a), (c), and (e) reveal the response in the *x*-direction, and the others are in the *y*-direction. The results reveal that a smaller *M* value and a larger *B* value result in faster response and less overshoot. When *K* increases, the system overshoot decreases. However, *K* does not affect the settling time. A larger *K* provides more stiffness, leading to worse compliance performance. The result of Fig. 11 provides a primary method for experiment parameter tuning.

Fig.12(a)-(f) demonstrate the numerical validation results of the compliance control. The results indicate the two compliance control methods have similar trends for adjusting parameters *B* and *M*. It is noteworthy that the increase of parameter *K* leads to a smaller maximum overshoot, which functions similarly to the spring constant in the system. The value of *K* should be reduced to increase compliance performance, and the value of *B* should be increased to reduce system overshooting and adjust the compliance performance of the system. Lastly, the parameter *M* is fine-tuned in the control system to achieve a more stable control.

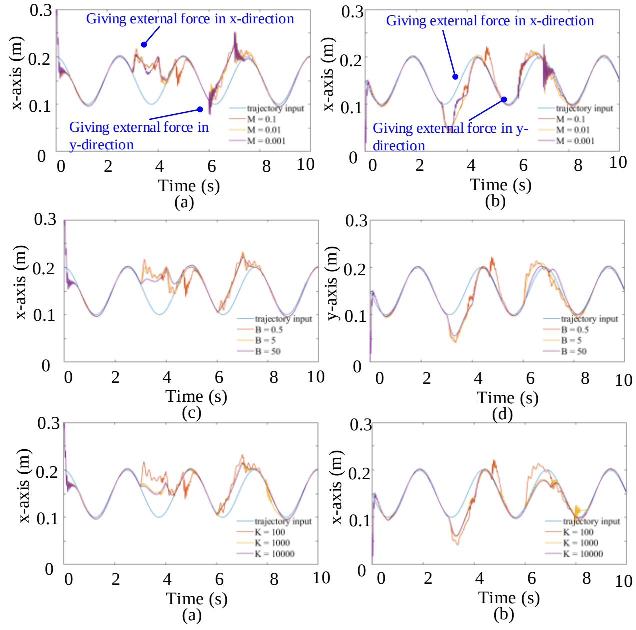

Fig. 12. Responses of the impedance compliance control of adjusting *M*, *B*, *K* parameters. (a), (b) Adjusting value of *M*. (c), (d) Adjusting value of *B*. (e), (f) adjusting value of *K*.

IV. EXPERIMENTAL VALIDATION OF THE DUAL-JOINT HDA SYSTEM

The HDA model, CSG-17-100-2UH-LW from Harmonic Drive Company, was used in the experiment, which has a ratio of one hundred to one and a lightweight design. The Maxon EC 60 flat brushless motor is produced by MAXON and is equipped with a Hall sensor and cable. The Hall sensor acquires motor output angular displacement, velocity, and acceleration information. The relevant parameters of the motor can be referred to in Table II. The EPOS4 Compact 50/15 CAN controller is paired with the motor, and the Communication is established via CANopen. The six-axis force and torque sensors manufactured by G4 Technology is utilized to measure force and torque by measuring the angular displacement between the upper and lower parts of the sensor. The angular displacement and torque sensor require an accurate reading of the output angle of the HDA's end. An optical disc is selected as the device for output angle measurement, and a read head is employed to capture digital displacement signals. Both components need to maintain a distance of 2.5 cm. National Instruments (NI) compactRio is used as the controller.

TABLE II
PARAMETERS OF THE DC MOTOR

Motor inertia J_m (gcm^2)	835	Input current I_0 (mA)	493
Torque constant k_m (mN·m/A)	52.5	Motor speed n_0 (rpm)	3730
Maximum radial load F_{max} (N)	110	Maximum efficiency $_{max}$ (%)	85

A. Experimental Validation of Torque Estimation

The experiment's objectives include: 1) Investigating the influence of kinematic torsion on torque estimation. 2) Validating equations (22) and (23), converting the measured force at the endpoint into torque, and comparing it with the estimated torque values for each axis. The experimental setup used in this section is illustrated in Fig.13.

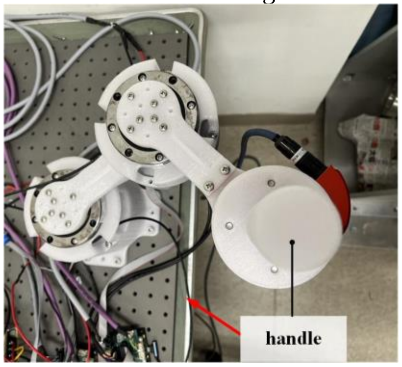

Fig. 13. Dual-joint Torque Estimation Experiment Setup

1) Kinematic torsion

Tolerance occurs in the HDA and DC motor assembly. As a result, the kinematic torsion results in periodic variations in the total twist angle of the HDA during rotation. Different magnitudes and directions of input torque are applied to the motor to investigate the kinematic torsion. The experimental results of kinematic torsion and flexible spline output angle are used to fit in the curve. The results are depicted in Fig. 14(a) and (b). Torques of 0.025(Nm), 0.03(Nm), and 0.035 (Nm) are applied clockwise and counterclockwise for the flex spline to rotate one revolution. The curve fitting coefficients for kinematic torsion are $[a_0, a_1, a_2, a_3, a_4, a_5]^T=[6.57\times10^{-5}, 0.0018, 0.0032, -0.0017, 2.68\times10^{-4}, -1.27\times10^{-4}]^T$ and $[b_0, b_1, b_2, b_3, b_4, b_5]^T=[1.72\times10^{-4}, 9.47\times10^{-4}, -0.0017, 3.47\times10^{-4}, 7.94\times10^{-4}, -3.67\times10^{-4}]^T$. Fig. 14 shows that the kinematic torsion and the flexible wheel output angle remain the same under different input torques.

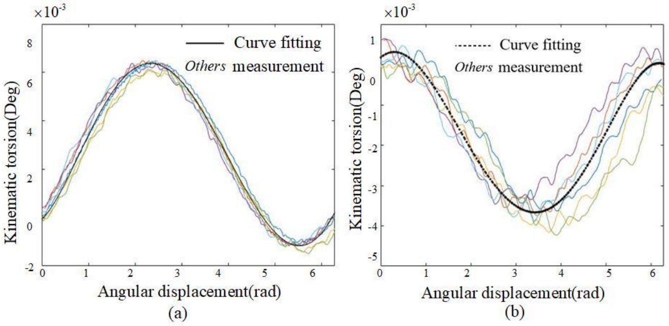

Fig. 14. Comparison of kinematic torsion and flexible wheel output angular displacement. (a) First-axis HDA. (b) Second-axis HDA.

2) Dual-joint robotic arm torque estimation

The experimental setup of dual-joint torque estimation is shown in Fig. 15(a), with force applied to the endpoint handle. Fig. 15(b) shows the experimental results of two scenarios. In the first scenario, no current is input to the motor of the second axis, and an external force is applied to the handle. The estimated torque follows a consistent trend with the twist angle. The points where the twist angle is zero correspond to moments when no force is applied. The torque estimation and twist angle curves exhibit similar peak noise, with noise appearing at relatively flat portions of the curve. That may be caused by the twist angle approaching zero when the torque remains constant, and the high resolution of the optical encoder makes it difficult to conduct interpolation. In the second scenario, a torque of 0.4 Nm is applied to the motor to initiate rotation, and an external force is applied to the endpoint handle, which is demonstrated at the bottom of Fig. 15(b).

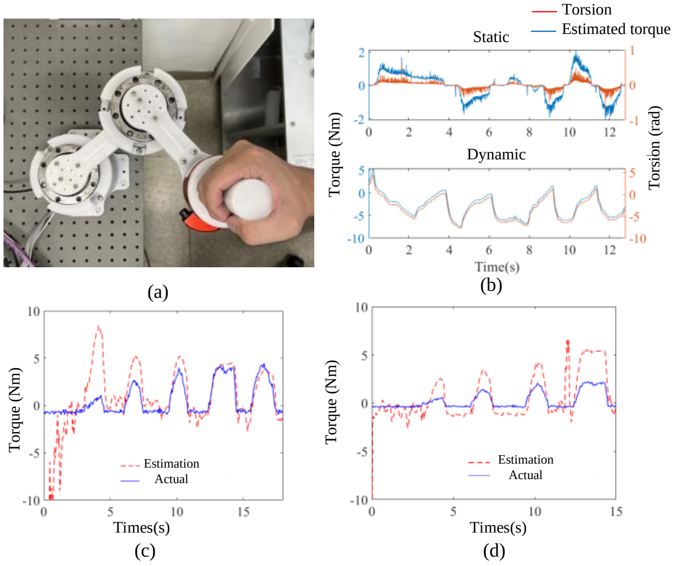

Fig. 15. Illustration of the dual-joint torque estimation and results. (a) Experimental setup. (b) Static and kinematic torque estimation. (c, d) Comparison of the estimated and actual torque for the first and second arm.

The six-axis force and torque sensor acquire the actual external force magnitude at the end-effector. The torque for each axis is determined through the force transformation in (22) and (23). Fig. 15(c) and (d) compare the estimated and actual torque estimation results when the motor gives 4 Nm of torque. Initially, there are significant errors, possibly due to the tolerance between the optical encoder and the optical disc, leading to inaccurate twist angle readings. However, after the system is stable, the overall torque estimation results closely match the actual values. It is observed that the torque estimation results for the second axis follow a similar trend to the actual values. Therefore, the torque estimation results of the dual-axis arm can be used as feedback signals for compliant control.

B. Experimental Validation of Compliance Control

The experimental setup of the robotic arm, angular displacement and torque sensors, and six-axis force and torque sensor are depicted in Fig. 16. The torque estimation values and the angular displacement information obtained from the optical encoder are input into the impedance controller. The parameters of the admittance and impedance compliance control used in the experimental validation are listed in Table III. In the experiment, the robot arm is disturbed by external force in *X* and *Y*-directions. The results of the compliance control experiment are shown in Fig. 16.

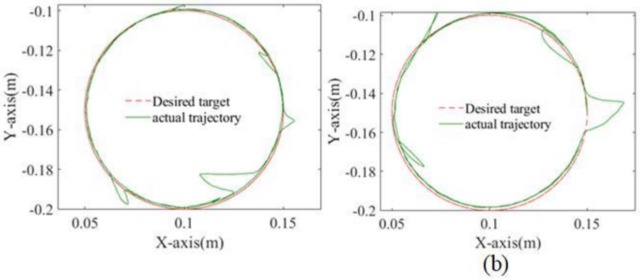

Fig. 16. Result demonstration of the compliance control. (a) impedance control. (b) compliance control.

TABLE III
PARAMETERS OF THE COMPLIANCE CONTROL
FOR EXPERIMENTAL VALIDATION

	Impedance compliance control	Admittance compliance control
M (kg)	0.001	1000
B(Ns/m)	10^{-10}	0.5
K(N/m)	10^{-5}	10

TRACKER software is utilized to track the trajectory by recording experiments. The robotic arm is commanded to draw a circle with a radius of five cm three times. No external force is applied during the first and third experiments, while an external force is applied during the second experiment. The comparison of trajectories before and after applying the force is demonstrated in Fig. 17. Figs. 17(a) and (b) depict the position-tracking results for impedance compliance control, and Fig. 17(c) and (d) are for admittance compliance control. Table IV presents the tracking errors. Both controllers exhibit similar position-tracking results and can successfully track back to the circular trajectory.

TABLE IV
PARAMETERS OF THE COMPLIANCE CONTROL
FOR EXPERIMENTAL VALIDATION

	Impedance compliance control		**Admittance compliance control**	
	X axis(mm)	Y axis(mm)	X axis(mm)	Y axis(mm)
Max error	3.1	3.6	3.4	3.7
Mean error	1.5	0.3	0.4	1.5
std	2.4	1.8	1.7	0.8

The method for designing controller parameters for impedance and admittance compliance controllers involves applying parameters obtained from simulations. LabVIEW software is utilized to monitor experimental data. A collision experiment, as depicted in Fig. 18, has been conducted to assess the compliance controllers' compliance performance after parameter adjustments. The experiments involve providing the arm with a circular trajectory with a radius of five centimeters and placing an obstacle along the path. The obstacle is a six-liter water bottle, simulating a scenario where a person is standing on the arm's trajectory, resulting in a new trajectory to accommodate the obstacle. Fig. 18(a) shows a side view of the experimental setup, while Fig. 18(b) depicts a plan view.

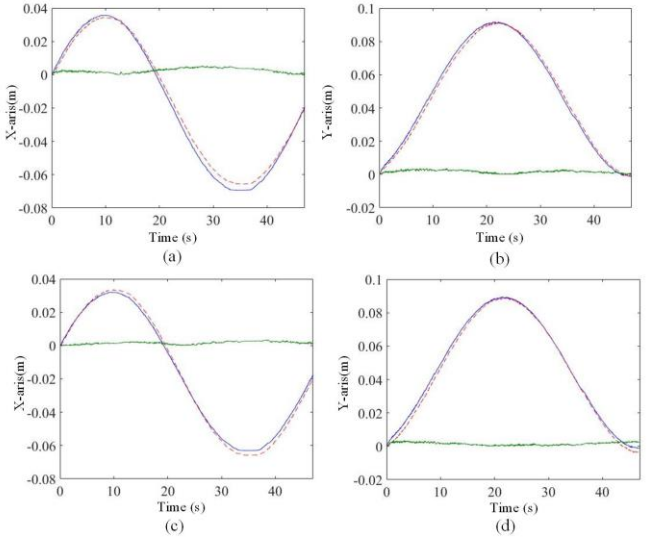

Fig. 17. Experimental results of the trajectory tracking. (a)-(b) impedance compliance control in X and Y-direction. (c)-(d) admittance compliance control in X and Y-direction.

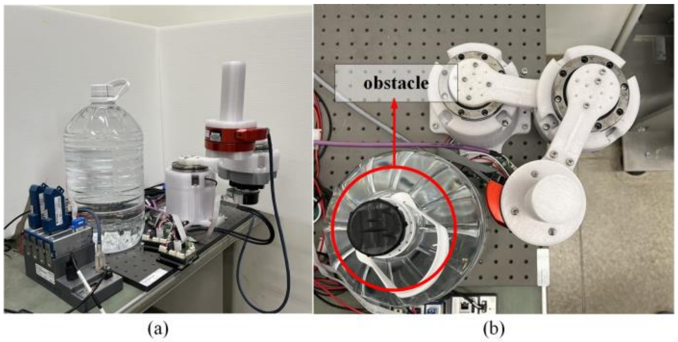

Fig. 18. Collision experimental setup for compliance control methods. (a) side view. (b) top-down view.

Three sets of parameters listed in Table V for each controller are utilized to investigate the impact of the controller parameters experimentally. Fig. 19(a) and (b) display the trajectory along the *x*-axis, and *y*-axis for admittance compliance control. The results suggest that Controller 3 exhibits higher compliance. By reducing the system's elasticity, larger displacements can be achieved. *B* is increased to prevent these larger displacements from affecting the arm's convergence to the original trajectory.

TABLE V
PARAMETERS OF THE COMPLIANCE CONTROL EXPERIMENTAL VALIDATION

Admittance compliance control			
Controller1	500	0.5	100
Controller 2	500	1	10
Controller 3	500	2	1
Impedance compliance control			
Controller 1	1	10^{-10}	10^{-5}
Controller 2	1.5	10^{-7}	10^{-12}
Controller 3	2	10^{-4}	10^{-22}

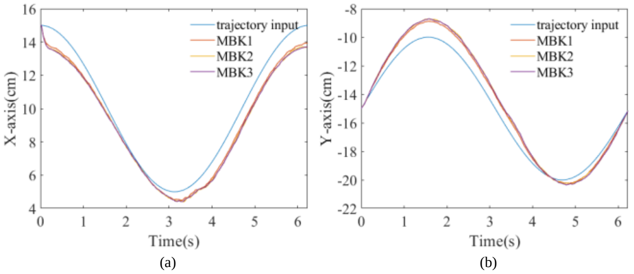

Fig. 19. Collision experimental results for admittance compliance control. (a) *X*-direction. (b) *Y*-direction.

Fig. 20 shows the experimental results of impedance compliance control. Increasing the damping coefficient *B* and decreasing the spring coefficient *K* allows for better arm compliance and reduces arm vibration.

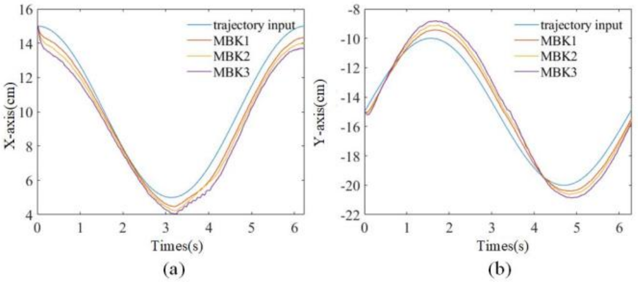

Fig. 20. Collision experimental results for impedance compliance control. (a) *X*-direction. (b) *Y*-direction.

From the results shown in Fig. 19 and Fig. 20, in the *x*-direction, there is a more noticeable error at the beginning with control operations due to the influence of the starting torque on the harmonic drive, causing significant vibration in the arm. As the arm's compliance increases, the vibration's amplitude becomes more significant. The angular displacement after collision using the impedance controller is less significant than the admittance controller. Fig. 21 compares the positions when the compliance effects of impedance and admittance control are similar. The parameters for the impedance controller are (M, B, K)= (0.0015kg, 10^{-7} N·s/m, 10^{-12} N/m) and (M, B, K) = (500 kg, 1 N·s/m, 10 N/m) for the admittance controller, Collision experiments were conducted with the parameter set.

When colliding with obstacles, the position tracking results of both controllers are similar, with an average position error of 0.135 mm. An approximate inverse relationship can be observed through experimentation, but the actual relationship between the two parameters requires further consideration of other factors affecting the system.

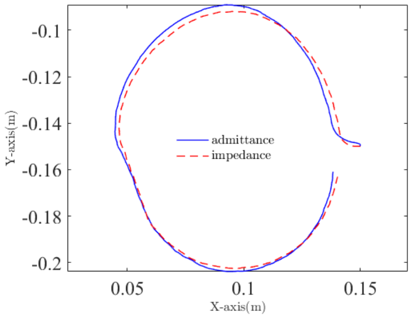

Fig. 21. Comparison of the compliance results from the impedance and admittance compliance control methods.

V. CONCLUSION

The development of a dual-joint HDA robotic arm system for compliant motion control is presented. This system can control motion and estimate torque, making human-robot interaction safer. The robotic arm system is modeled and verified through numerical simulation and experiments to validate the impedance and admittance control.

The developed torque estimation sensors can more accurately represent the flexible model of the harmonic drive, reducing interference in torque estimation through improvements in the mechanism. The torque sensing technique reduces overall arm production costs, simplifies arm complexity, and reduces overall weight. In addition to robotic applications, the estimation method can be used in automation equipment and machine tool industries. The fifth-order curve fitting is performed to compensate for the dynamic torsion angle. The compliant control methods are implemented in the dual-joint HDA robotic arm through the design of impedance and admittance controllers integrated into the dual-joint HDA arm model.

The parametric effects of the controller parameters are investigated. The dual-joint HDA robotic arm system is given a specific working path in simulation and experiments. External force is applied to observe the two controllers' compliance and position-tracking capabilities. To reduce the cost of development and verification, the mechanism hardware in this research is produced using 3D printing and has low stiffness. In the future, higher-stiffness materials, such as aluminum and iron, can be considered to reduce the backlash during the arm assembly process and decrease vibration during rotation. The estimation can be more accurate, and the robotic arm control can be improved. In addition, the proposed dual-joint HDA robotic arm system can be extended to multi-axis motion for more applications.

REFERENCES

[1] I. Godler, M. Horiuchi, M. Hashimoto, and T. Ninomiya, “Accuracy improvement of built-in torque sensing for Harmonic Drives," *IEEE/ASME Trans. on Mechatronics*, vol. 5, no. 4, pp. 360-366, Dec. 2000.

[2] D. Tsetserukou, R. Tadakuma, H. Kajimoto, N. Kawakami and S. Tachi, “Intelligent variable joint impedance control and development of a New Whole-Sensitive Anthropomorphic Robot Arm," in *Int. Symp. Comput. Intell. Robot. Autom.*, 2007, pp. 338-343.

[3] W. Li, Y. Han, J. Wu and Z. Xiong, "Collision Detection of Robots Based on a Force/Torque Sensor at the Bedplate," *IEEE/ASME* Transactions *on Mechatronics*, vol. 25, no. 5, pp. 2565-2573, Oct. 2020.

[4] A. Calanca, R. Muradore and P. Fiorini, "A Review of Algorithms for Compliant Control of Stiff and Fixed-Compliance Robots," *IEEE/ASME* Transactions *on Mechatronics*, vol. 21, no. 2, pp. 613-624, April 2016.

[5] A. -N. Sharkawy, P. N. Koustournpardis and N. Aspragathos, "Variable Admittance Control for Human-Robot Collaboration based on Online Neural Network Training," in *IEEE/RSJ Int. Conf. Intell. Robots Syst*., 2018, pp. 1334-1339.

[6] M. Sharifi, A. Zakerimanesh, J. K. Mehr, A. Torabi, V. K. Mushahwar and M. Tavakoli, "Impedance Variation and Learning Strategies in Human–Robot Interaction," *IEEE Transactions on Cybernetics*, vol. 52, no. 7, pp. 6462-6475, July 2022.

[7] T. Sun, L. Peng, L. Cheng, Z. -G. Hou and Y. Pan, "Stability-Guaranteed Variable Impedance Control of Robots Based on Approximate Dynamic Inversion," *IEEE Transactions on Systems, Man, and Cybernetics: Systems*, vol. 51, no. 7, pp. 4193-4200, July 2021.

[8] C. Caulcrick, W. Huo, W. Hoult and R. Vaidyanathan, "Human Joint Torque Modelling With MMG and EMG During Lower Limb Human-Exoskeleton Interaction," *IEEE Robotics and Automation Letters*, vol. 6, no. 4, pp. 7185-7192, Oct. 2021.

[9] A. Ghaffar, M. Z. U. Rahman, V. Leiva, C. Martin-Barreiro, I. Ali, X. Cabezas, and C. Castro, “Efficiency, optimality, and selection in a rigid actuation system with matching capabilities for an assistive robotic exoskeleton” *Eng. Sci. Technol.*, vol. 51, no. 101613, pp. 1-12, Mar. 2024.

[10] B. Huang, Z. Ye, Z. Li, W. Yuan and C. Yang, "Admittance control of a robotic exoskeleton for physical human robot interaction," in *Int. Conf. Adv. Robot. Mechatron.*, 2017, pp. 245-250.

[11] B. Ugurlu, H. Oshima, E. Sariyildiz, T. Narikiyo and J. Babic, "Active Compliance Control Reduces Upper Body Effort in Exoskeleton-Supported Walking," *IEEE Trans. Hum.-Mach. Syst.*, vol. 50, no. 2, pp. 144-153, April 2020.

[12] T. Huang, K. Chen and J. F. Pan, "Admittance Control of Dual-arm Cooperative Platform," in *Int. Conf. Power Electron. Syst. Appl*., 2022, pp. 1-5.

[13] J. Cacace, R. Caccavale, A. Finzi and V. Lippiello, "Variable Admittance Control based on Virtual Fixtures for Human-Robot Co-Manipulation," in *IEEE Int. Conf. Syst. Man Cybern.*, 2019, pp. 1569-1574.

[14] G. E. Dongming, S. Guanghui, Z. Yuanjie and S. Jixin, "Impedance control of multi-arm space robot for the capture of non-cooperative targets," *J. Syst. Eng. Electron*., vol. 31, no. 5, pp. 1051-1061, Oct. 2020.

[15] N. M. Kircanski, and A. A. Goldenberg,” An Experimental Study of Nonlinear Stiffness, Hysteresis, and Friction Effects in Robot Joints with Harmonic Drives and Torque Sensors,” *Int. J. Robot. Res.*, vol. 16, no. 2, pp.214-239, Apr. 1997.

[16] R. Dhaouadi, F. H. Ghorbel and P. S. Gandhi, "A new dynamic model of hysteresis in harmonic drives," *IEEE Trans. Ind. Electron.*, vol. 50, no. 6, pp. 1165-1171, Dec. 2003.

[17] T. W. Nye, and R. P. Kraml, “Harmonic Drive Gear Error: Characterization and Compensation for Precision Pointing and Tracking”, in *Aero. Mech. Symp. NASA*, 1991, pp.237-252.

[18] T. D. Tuttle. “Understanding and Modeling the Behavior of a Harmonic Drive Gear Transmission,” MIT Artificial Intelligence Laboratory, MA, USA, Tech. Rep. AD-A259 610, May 1992.

[19] C. Preissner, and T. J. Royston, “A High-Fidelity Harmonic Drive Model”, *J. Dyn. Syst. Meas. Control*, vol. 134, no. 011002, pp. 1-13, Jan. 2012.

[20] Li, “Torque Estimation Technique for Feedback Control of Harmonic Drive Actuator,” M.S. thesis, Dept. Mech. Eng., National Taiwan Univ., Taipei, Taiwan, July, 2021.

[21] H. Zhang, S. Ahmad and G. Liu, "Modeling of Torsional Compliance and Hysteresis Behaviors in Harmonic Drives," *IEEE/ASME Trans. on* Mechatronics, vol. 20, no. 1, pp. 178-185, Feb. 2015.

[22] S. Oh and K. Kong, "High-Precision Robust Force Control of a Series Elastic Actuator," *IEEE/ASME Trans. on Mechatronics*, vol. 22, no. 1, pp. 71-80, Feb. 2017.

[23] T. T. Phuong, K. Ohishi, Y. Yokokura and Y. Takei, "Applications of disturbance observer and kalman filter based force sensation in motion control," in *IEEE Int. Workshop Adv. Mot. Control*, 2018, pp. 625-630.

[24] M. A. A. Ismail, J. Windelberg and G. Liu, "Simplified Sensorless Torque Estimation Method for Harmonic Drive Based Electro-Mechanical Actuator," *IEEE Robot. Autom. Lett*., vol. 6, no. 2, pp. 835-840, April 2021.

[25] N. Kashiri, J. Malzahn and N. G. Tsagarakis, "On the Sensor Design of Torque Controlled Actuators: A Comparison Study of Strain Gauge and Encoder-Based Principles," *IEEE Robot. Autom. Lett.*, vol. 2, no. 2, pp. 1186-1194, April 2017.

[26] Y. B. Kim, U. Kim, D. -Y. Seok, J. So, Y. H. Lee and H. R. Choi, "Torque Sensor Embedded Actuator Module for Robotic Applications," *IEEE/ASME Trans. on Mechatronics*, vol. 23, no. 4, pp. 1662-1672, Aug. 2018.

[27] H. D. Taghirad and P. R. Belanger, "Intelligent built-in torque sensor for harmonic drive systems," *IEEE Trans. Instrum. Meas.*, vol. 48, no. 6, pp. 1201-1207, Dec. 1999.

[28] J. W. Sensinger and R. F. Weir, "Improved torque fidelity in harmonic drive sensors through the union of two existing strategies," *IEEE/ASME Trans. Mech.*, vol. 11, no. 4, pp. 457-461, Aug. 2006.

[29] D. Yamada, J. Huang, and T. Yabuta, " Comparison between admittance and impedance control of a multi-finger-arm robot using the guaranteed manipulability method," Precis. Instrum. Mecanology., vol. 2, no. 2, pp. 85–93, Jul. 2013.

[30] F. H. Ghorbel, P. S. Gandhi, and F. Alpeter, "On the Kinematic Error in Harmonic Drive Gears ." *ASME. J. Mech. Des.*, vol. 123, no. 1, pp. 90–97, Mar. 2001.

[31] "Fine *mechanics & total motion control HarmonicDrive*", HASEGAWA Corp., Chiba, Japan, 2018.

Wen-Hao Chen received a B.S. degree in mechanical engineering from National Sun Yat-sen University, Taiwan, in 2021, and the M.S. degree in mechanical engineering from National Taiwan University, Taipei, Taiwan, in 2023. He is currently an process engineer at Taiwan Semiconductor Manufacturing Company. His current research interests include robotics and mechatronics.

Yu-Han Tsai received a B.S. degree in Mechanical engineering from the National Taiwan University, Taipei, Taiwan in 2023. He is currently pursuing a Ph.D. degree in Mechanical engineering. His current research interests include magnetic tracking systems, robotics, and mechatronics.

Chun-Yeon Lin (Member, IEEE) received the B.S. degree in mechanical engineering from National Central University, Taoyuan, Taiwan, in 2003, the M.S. degree in electrical control engineering from National Chiao Tung University, Hsinchu, Taiwan, in 2005, the M.S. degree in mechanical engineering from Stanford University, Stanford, CA, USA, in 2011, and the Ph.D. degree in mechanical engineering from Georgia Institute of Technology, Atlanta, GA, USA, in 2017. He is currently an Associate Professor at the Department of Mechanical Engineering, National Taiwan University, Taipei, Taiwan. His current research interests include mechatronics, sensing systems, robotics, and system dynamics and control.